Hindawi
Shock and Vibration
Volume 2022, Article ID 4718228, 17 pages
https://doi.org/10.1155/2022/4718228

Research Article

Experiment and Simulation on the Anticollision Performance of a New Corrugated Steel Protection System for Bridge Piers

Guicheng Chen, Haidong Huang, and Zhongfu Xiang

School of Civil Engineering, Chongqing Jiaotong University, Chongqing 400074, China

Correspondence should be addressed to Guicheng Chen; chenguicheng968@163.com

Received 21 October 2021; Revised 15 May 2022; Accepted 29 June 2022; Published 22 July 2022

Academic Editor: Fabio Minghini

To ensure the safety of ships and bridges at the same time during collisions, a new type of bridge pier protection system is proposed, in which one is composed of corrugated steel plates, bolts, and corrugated steel pipes (CSP), and the other is composed of ordinary steel plates, bolts, and corrugated steel pipes (OSP). To study their anticollision performance, a pendulum impact test and numerical simulation were carried out. Comparing the test results with the simulation results, it was shown that the simulation results are basically consistent with the test results. Then, the influence curves of the impact velocity, specimen thickness, weight, and frequency are analysed to evaluate the anticollision performance of CSP/OSP and optimize their structure. When the impact energy is low, the peak values of the lateral impact force and lateral displacement of the column equipped with OSP are all smaller than those of the column equipped with CSP. When the impact energy is high, the peak values of the lateral impact force and lateral displacement of the column equipped with OSP are larger than those of the column equipped with CSP. However, under the same impact energy, the total energy peak value of the CSP specimen is larger than that of the OSP specimen. Results can provide a certain numerical analysis basis for the structural design and research of new types of corrugated steel protection system for bridge pier.

1. Introduction

The accident of a ship hitting a bridge pier causes serious economic losses and casualties [1,2]. Especially with the increasing number of ships and their upsizing, the probability and risk of bridge piers being impacted have gradually increased. Therefore, bridges crossing inland waterways and coastal waterways must be designed to have anticollision properties. At present, two main ways are used to improve the impact resistance of bridges. One is to improve the impact resistance of the piers, and the other is to add anticollision facilities. During collisions, to ensure the safety of ships and bridges at the same time, adding anticollision facilities is feasible.

AASHTO [3] provides some classic anticollision systems such as baffle systems, pile support systems, artificial island systems, and floating protection systems. Chen [4] proposed two new protection methods, namely, new materials and flexible energy consumption. Peng [5] summarized the development of anticollision facilities in 25 years, gave the application scenarios of 18 anticollision facilities in different regions, and compared the impact force changes before and after the addition. Chen [6] designed a new device to prevent ships from colliding with bridge piers called a flexible steel rope anticollision device. Jiang et al. [7] used a new material FRP to design an anticollision pontoon. Zhou et al. [8] proposed a steel-CFRP combined with an anticollision box. Shan and Huang [9] proposed a curve-shaped anticollision floating box of a bridge pier with a sandwich structure. These types of anticollision facilities have good anticollision effects and can effectively reduce the impact force during an impact. However, the cost is relatively high, the production process is complicated, they are difficult to industrialize, and the construction period is long. The honeycomb structure has good energy absorption and dissipation characteristics [10–12] and is an excellent type of anticollision facility

structure. A new type of honeycomb pier anticollision facility with corrugated steel plates, bolts, and corrugated steel pipes (CSP) or ordinary steel plates, bolts, and corrugated steel pipes (OSP) as the structural element is proposed. It absorbs energy through the deformation of corrugated steel plates (or ordinary steel plates) and corrugated steel pipes, prolonging the impact time and reducing the impact force.

Corrugated steel is widely used in engineering fields such as pipelines, culverts, buildings, and bridges. Fang et al. [13] analysed the axial mechanical behaviour of concrete-filled corrugated steel tube columns. Nassirnia et al. [14] proposed a hollow corrugated column by incorporating ultra-high-strength steel tubes and analysed its compression behaviour and buckling shape under axial load. Wojcik et al. [15] conducted full-scale filling and emptying tests on a medium-size steel cylindrical flat bottom silo with horizontally corrugated walls and columns composed of open-sectional thin-walled profiles, and the test results were different from those of Eurocode1. Kearns et al. [16] used simulated vehicle loads to conduct experimental research on corrugated steel ellipse culverts. The test results showed that the bending moment seriously affects the bearing capacity of corrugated steel ellipse culverts. Garcia and Moore [17] conducted laboratory tests on the joints in buried gravity flow pipelines to obtain the failure mode. Beben [18] studied the effect of backfill quality on corrugated steel plate culverts using three-dimensional numerical simulation and experimental comparison. Li et al. [19] used experimental methods to study an existing rehabilitated reinforced concrete rehabilitated with a grouted corrugated steel pipe. Regier et al. [20] conducted experimental research on deteriorated corrugated steel pipes, and the results showed that the corrosion level affects the bearing capacity of corrugated steel culverts. Yang et al. [21] used parametric numerical simulations to simulate the mechanical behaviour of helical corrugated steel pipes under axial tension, bending, and internal pressure loads and combined the simulations with a multiobjective optimization algorithm to propose an optimization method for the structural design of liquefied natural gas cryogenic helical corrugated pipes. Guo et al. [22] analysed the characteristic buckling of the concrete-infilled double steel corrugated-plate wall and studied its overall elastic buckling behaviour under axial load. Wang et al. [23] proposed a new type of shear wall with concrete-filled steel tubular frames and a corrugated steel plate and studied its seismic performance. Zhu et al. [24,25] conducted experiments and numerical studies on concrete-infilled double steel corrugated-plate walls, and the results showed that the walls had good seismic performance and bearing capacity. Wang et al. [26,27] used comparative experiments and numerical analysis methods to analyse the axial load-bearing characteristics and bending-torsion characteristics of concrete-infilled double steel corrugated-plate walls with T-section. Leblouba et al. [28,29] studied the shear characteristics of corrugated web steel beams. Zhou et al. [30] studied the torsion behaviour of prestressed composite box girders with corrugated steel webs. Zhou and An [31] studied the shear performance of nonprismatic beams with steel trapezoidal corrugated webs by numerical simulation and experiment. He et al. [32,33] conducted model tests on composite box girders with corrugated webs and steel tube slabs to study their structural damage mechanisms. Si et al. [34] analysed the difference in the dynamic response of deck pavement of two kinds of box girder bridges. Maslak et al. [35] used experimental and numerical analysis methods to study the steel corrugated arch sheets exposed to fire. Wu et al. [36] used numerical analysis and test methods to study the buckling behaviour and failure mode of steel circular closed supports with I-sections of sinusoidal corrugated webs. Fan et al. [37] used impact tests and finite element methods to study the anti-collision performance of UHPFRC-based protective structures for bridge columns. Zhao et al. [38] conducted a combined test study of the axial and horizontal cyclic load on corrugated double-skin composite walls. Niknejad et al. [39] used quasi-static test methods to study the energy absorption characteristics of circular corrugated tubes under axial and lateral pressure. Studies have shown that corrugated steel plates or corrugated steel pipes have good characteristics such as shear resistance, bending resistance, torsion resistance, seismic resistance, and energy absorption, but the anticollision performance has not been studied in depth, so numerical simulation research on its anticollision performance has a major significance.

In summary, this paper carries out numerical simulation research according to the pendulum impact test and studies the anticollision performance of CSP/OSP specimen. In addition, the relationship curve between the CSP/OSP specimen thickness and the peak value of the simulation results is analysed to evaluate the anticollision performance of CSP/OSP and its energy dissipation effect. The research results can provide a certain theoretical and experimental basis for the design and analysis of the two types of corrugated steel protection system for bridge pier.

2. Establishment and Verification of the Numerical Model of Pendulum Impact Test

In order to accurately evaluate the anticollision performance of the CSP/OSP specimens, a finite element model is established according to the geometric structure of the pendulum impact test for numerical simulation, and the entire pendulum impact test process is analysed in detail.

2.1. Pendulum Impact Test. The setting, data acquisition and processing, test phenomena, test results, and analysis of pendulum impact test have been introduced and discussed in detail in [40], which will not be repeated here.

2.2. Geometric Structure. The geometric structure of the CWACF-12.0 specimen is shown in Figure 1(a). Waveform parameter of the corrugated steel plate (wave distance × wave depth) is 400 mm × 150 mm, and that of the corrugated steel pipe is 200 mm × 55 mm. The geometric structures of the CSP and OSP specimens are shown in Figures 1(b) and 1(c), respectively.

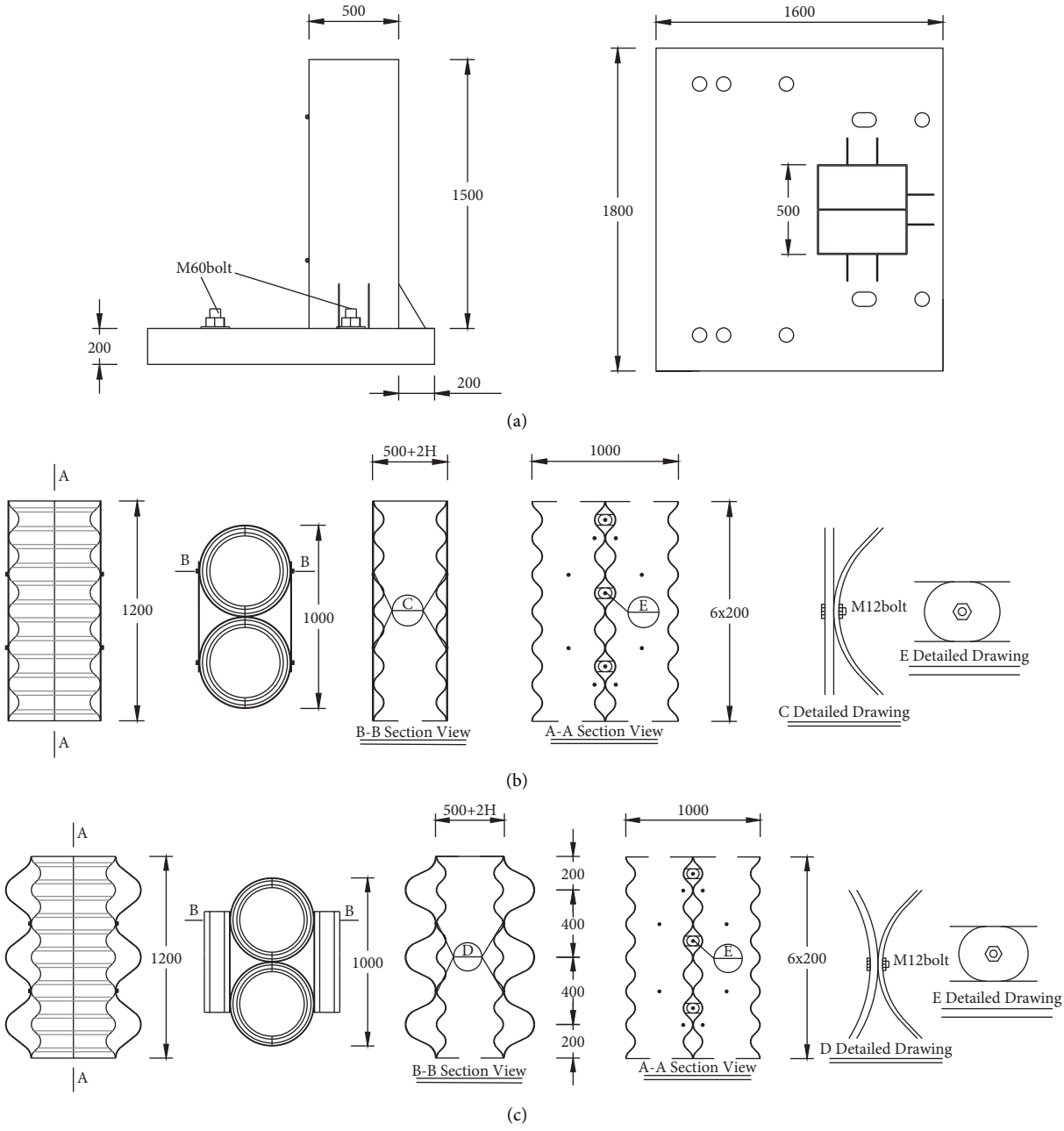

Figure 1: Geometry of the specimen (unit: mm). (a) CWACF-12.0 specimen geometry. (b) OSP specimen geometry. (c) CSP specimen geometry.

2.3. Finite Element Model. Huang et al. [41] analysed the anticollision performance of flexible anticollision rings in different operating conditions through numerical simulation and experiments. Zhang et al. [42] used scale model tests and three-dimensional numerical models to analyse the failure modes of segmented precast columns under impact loads. Do et al. [43] used the pendulum impact test and numerical simulation to study the failure mode of a car hitting a bridge pier. Zhang and Hu [44] obtained the mechanical properties of bolt splicing through accurate finite element analysis and proposed a feasible simplified simulation method for bolts. Zhang et al. [42] used bolts to connect the impact test model to the bottom of the laboratory. Under the pretightening force of the bolts, the bottom of the model column did not move or rotate.

ANSYS/LS-DYNA is a display dynamics program based on a display solution, suitable for solving impact and collision problems. The steel plate and the corrugated steel pipe are connected by high-strength bolts. In the numerical simulation, the high-strength bolts are simplified to the beam element, and the beam element algorithm SPOTWELD-BEAM is called in combination with the keyword *INITIAL_AXIAL_FROCE_BEAM to apply pretightening force. The bolt pretightening force setting is assembled

Table 1: Composition of the finite element model.

Component	Element	Element formulation	Size	Total number
Base	Solid	2	12 mm × 12 mm × 12 mm	58607
Column	Solid	2	12 mm × 12 mm × 12 mm	26795
Pendulum	Solid	2	12 mm × 12 mm × 12 mm	6360
M12	Beam	9	1.2 mm	45
M60	Beam	9	6 mm	220
Corrugated steel plate	Shell	2	12 mm × 12 mm	20248
Corrugated steel pipe	Shell	2	12 mm × 12 mm	26229
Ordinary steel plate	Shell	2	12 mm × 12 mm	10176
Floor	Shell	2	30 mm × 30 mm	1593
Approach slab	Shell	2	10 mm × 10 mm	567

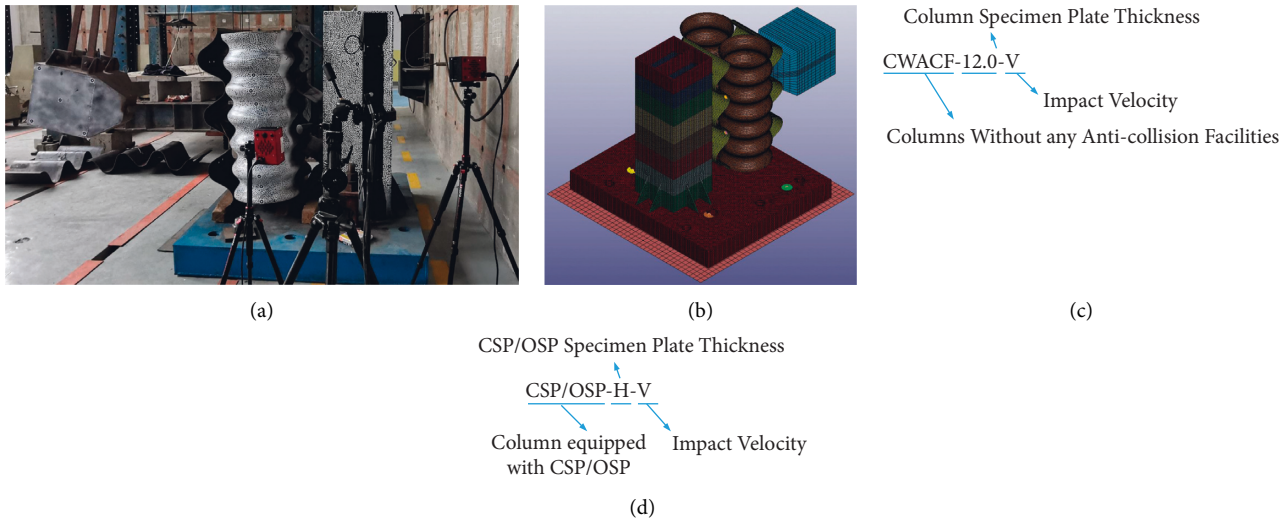

Figure 2: Description of model and case number. (a) Field test model of CSP-2.75-4; (b) finite element model of CSP-2.75-4; (c) description of the case number of the column without anticollision facilities; (d) description of the case number of the column equipped with CSP/OSP.

according to the impact test specimen. In the numerical simulation, the pretightening forces of M60 high-strength bolts and M12 high-strength bolts are set to 100 and 50 N, respectively. The connection between bolts and steel plates and steel pipes can be realized through the keyword *CONSTRAINED_NODAL_RIGID_BODY. The coefficients of static friction and dynamic friction between steels are 0.2 and 0.1, respectively. The static and dynamic friction coefficients of the base and the laboratory floor are set to 0.8 and 0.6, respectively, according to the friction coefficient [45] between iron and rubber to increase its relative sliding resistance. The contact between the pendulum and the steel plate, the contact between the steel plate and the column, and the contact between the base and the laboratory floor can be realized through the keyword *CONTACT_AUTOMATIC_SURFACE_TO_SURFACE. The self-contact between the steel plate and the corrugated steel pipe can be realized through the keyword *CONTACT_AUTOMATIC_SINGLE_SURFACE. The boundary condition is set as that one end of the connection between M60 bolt and laboratory floor is consolidation constraint. The laboratory floor is treated as a fixed rigid part. The element grid data is summarized in Table 1. CSP-2.75-4 field test model and its corresponding finite element model are shown in Figure 2.

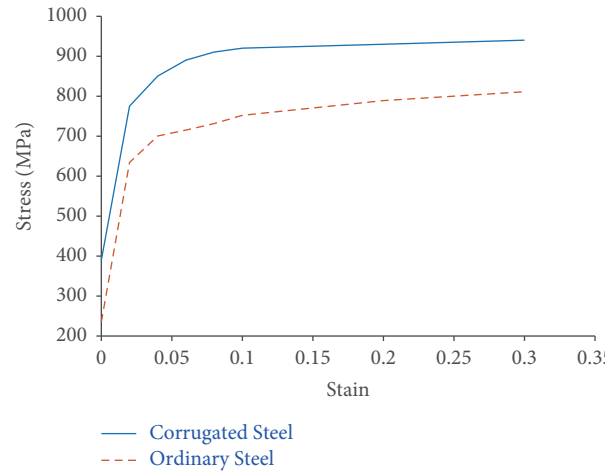

Figure 3: Stress-strain curve.

Table 2: Material characteristic parameters.

Material	LS-DYNA material model	Density	Young's modulus	Poisson's ratio	Yield stress
Corrugated steel	*MAT_PIECEWISE_LINEAR_PLASTICITY	7850 kg/m^3	176 GPa	0.31	390 MPa
Ordinary steel	*MAT_PIECEWISE_LINEAR_PLASTICITY	7850 kg/m^3	206 GPa	0.31	235 MPa
High-strength bolts	*MAT_SPOTWELD	7850 kg/m^3	206 GPa	0.30	640 MPa
Pendulum	*MAT_PLASTIC_KINEMATIC	3000 kg/m^3	206 GPa	0.31	1200 MPa
Laboratory floor	*MAT_RIGID	2600 kg/m^3	34.5 GPa	0.2	—

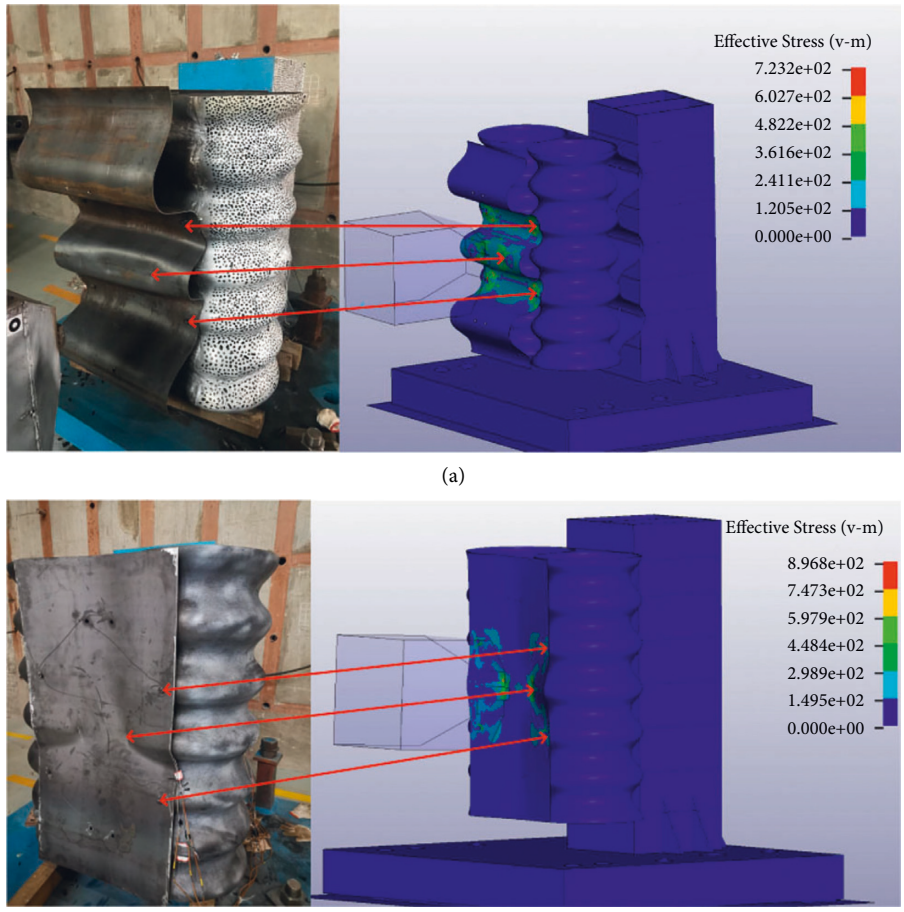

Figure 4: Deformation of steel plate at the impact. (a) CSP-2.75-4; (b) OSP-2.75-4.

2.4. Material Model. Zhi et al. [46], on the basis of the quasi-static tensile, high-temperature tensile, and dynamic tensile test data of Q235B, proposed that the Cowper-Symonds constitutive relationship in ANSYS/LS-DYNA is suitable for low-speed collisions in the engineering field. The material model *MAT_PLASTIC_KINEMATIC (MAT_003) in LS-DYNA can consider the influence of strain rate. Given that the corrugated steel plate and corrugated steel pipe are cold-formed [13], the yield strength is improved and the plasticity is reduced. The elastic-plastic material model *MAT_PIECE WISE_LINEAR_PLASTICITY (MAT_024) in ANSYS/LS-DYNA can consider the isotropic and kinematic hardening plasticity of the material, allowing the definition of any stress-strain relationship curve and the influence of strain rate. The influence of strain rate changes on the constitutive relationship of steel has been discussed by Kim et al. [47], Paik et al. [48], Park et al. [49], and Rokaya and Kim [50]. Figure 3 shows the stress-strain curve of the steel used in the numerical simulation based on the test measurement. The SPOTWELD-BEAM algorithm requires that it can only be used in conjunction with the material model *MAT_SPOT WELD (*MAT_100) in ANSYS/LS-DYNA, so this material model can only be used to define the constitutive relationship of the bolt. The laboratory floor is very rigid. When using shell element simulation, it will be regarded as a rigid body, so its material model is defined by *MAT_RIGID (MAT_001). The material characteristic parameters are shown in Table 2.

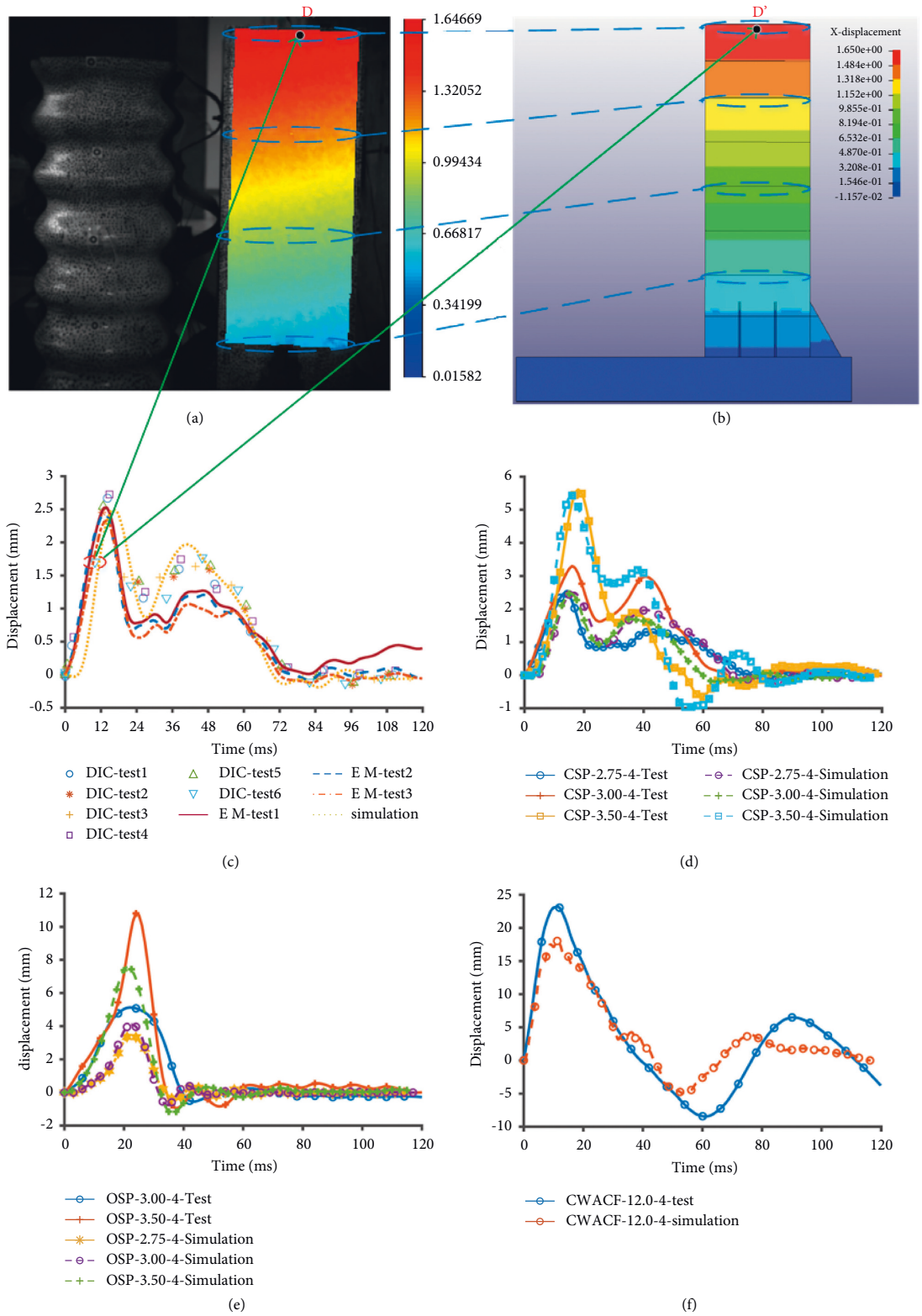

FIGURE 5: Comparison between experimental results and simulation results of lateral displacement field and lateral displacement time history curve of column (unit: mm). (a) The experimental result of CSP-2.75-4; (b) simulation result of CSP-2.75-4; (c) time history curve of CSP-2.75-4; (d) CSP; (e) OSP; (f) CWACF-12.0.

2.5. Model Calibration and Comparisons. The simulation results are verified by the impact test results provided in [40]. Taking CSP-2.75-4 and OSP-2.75-4 as examples, the deformation of the steel plate at the impact is shown in Figure 4. The experimental and simulation results of the deformation of the steel plate of CSP/OSP are basically

Table 3: Parameter study.

Number	H (mm)	V (m/s)	Weight (kg)	Peak displacement (mm)		Peak impact force (kN)			Peak total energy (J)	
				Test	Simulation	Pendulum-CSP/OSP	CSP/OSP-column	Pendulum-column	CSP/OSP	Column
CSP-2.75-2	2.75	2	131.06	1.27	1.07	38.23	44.08	—	845.70	16.49
CSP-3.00-2	3.00	2	145.90	1.41	1.11	45.90	50.87	—	827.96	22.371
CSP-3.50-2	3.50	2	166.96	2.79	2.66	59.80	97.99	—	742.15	64.57
OSP-2.75-2	2.75	2	118.04	—	1.08	56.64	33.8	—	762.85	16.37
OSP-3.00-2	3.00	2	129.26	1.29	1.04	59.47	30.95	—	786.06	16.90
OSP-3.50-2	3.50	2	145.40	2.08	2.20	64.37	33.51	—	748.68	37.08
CWACF-12.0-2	—	2	—	13.65	9.65	—	—	444.41	—	768.18
CSP-2.75-3	2.75	3	131.06	2.37	2.39	43.68	47.92	—	1859.13	46.39
CSP-3.00-3	3.00	3	145.90	2.32	2.34	52.95	55.11	—	1873.36	50.64
CSP-3.50-3	3.50	3	166.96	3.56	3.12	66.06	116.12	—	1811.08	91.85
OSP-2.75-3	2.75	3	118.04	—	2.62	123.53	72.56	—	1569.01	103.76
OSP-3.00-3	3.00	3	129.26	3.63	2.64	131.52	64.13	—	1567.23	106.00
OSP-3.50-3	3.50	3	145.40	5.21	4.51	111.60	61.51	—	1501.16	116.79
CWACF-12.0-3	—	3	—	17.28	13.97	—	—	644.64	—	1853.22
CSP-2.75-4	2.75	4	131.06	2.49	2.49	48.03	50.86	—	3326.84	48.07
CSP-3.00-4	3.00	4	145.90	3.32	2.47	56.70	58.06	—	3335.84	57.45
CSP-3.50-4	3.50	4	166.96	5.57	5.43	73.10	121.34	—	3213.86	143.00
OSP-2.75-4	2.75	4	118.04	—	3.47	158.53	83.86	—	2859.94	181.30
OSP-3.00-4	3.00	4	129.26	5.23	4.10	177.59	96.29	—	2653.40	256.23
OSP-3.50-4	3.50	4	145.40	10.83	7.61	185.703	97.38	—	2350.74	330.11
CWACF-12.0-4	—	4	—	23.40	18.08	—	—	793.83	—	3307.93

consistent. When the specimen thickness is the same, the deformation of the outer steel plate increases with the increase of the impact velocity. When the impact velocity is the same, the deformation of the outer steel plate decreases with the increase of the specimen thickness.

Taking the direction balanced with the initial impact velocity as the positive direction of the lateral displacement, the lateral displacement field and the time history curves of the lateral displacement at the top of the column are shown in Figure 5. Figure 5(c) shows that the trend of the time history curve of the lateral displacement at the top of the CSP-2.75-4 column is highly similar. The simulation and test results of the peak value of the lateral displacement of point D are 2.49 mm. The test results and simulation results of the lateral displacement field of the CSP-2.75-4 column at 10 ms are shown in Figures 5(a) and 5(b), respectively. The lateral displacement at the top position is 1.65 mm, that at the 3/4 position is 1.32 mm, that at the middle position is 0.986 mm, and that at the 1/4 position is 0.49 mm. It is shown that the test results of lateral displacement field of column are basically consistent with the simulation results.

Taking the impact velocity of 4 m/s as an example, the time history curves of the lateral displacement at the top of the column of CSP, OSP, and CWACF-12.0 obtained by the impact test and simulation are shown in Figures 5(d)–5(f), respectively. It is shown that the time of CSP column returning to the initial position is greater than that of OSP, and CSP/OSP can effectively reduce the peak value of the lateral displacement at the top of the column. With the increase of impact velocity, the peak value of the lateral displacement at the top of the column also increases. The smaller the plate thickness of CSP/OSP specimen, the smaller the peak value of the lateral displacement at the top of the column.

The comparison between the test results and simulation results of displacement and deformation fully shows that the established finite element model can accurately simulate the whole experimental process of pendulum impact.

3. Simulation Results

The time history curves and peak values of the lateral impact force, energy, and lateral displacement were obtained by numerical simulation. The anticollision performance of CSP/OSP under impact load is analysed and evaluated by comparing the simulation results under different case.

3.1. The Characteristics of the Lateral Displacement. The time history curves of the lateral displacement at the top of the column with impact velocity of 4 m/s are introduced in Section 2.5. The test results and simulation results of the lateral displacement peak values of each case are summarized in Table 3. The data shows that the experimental results are consistent with the numerical calculation results. As the impact velocity increases, the lateral displacement peak value

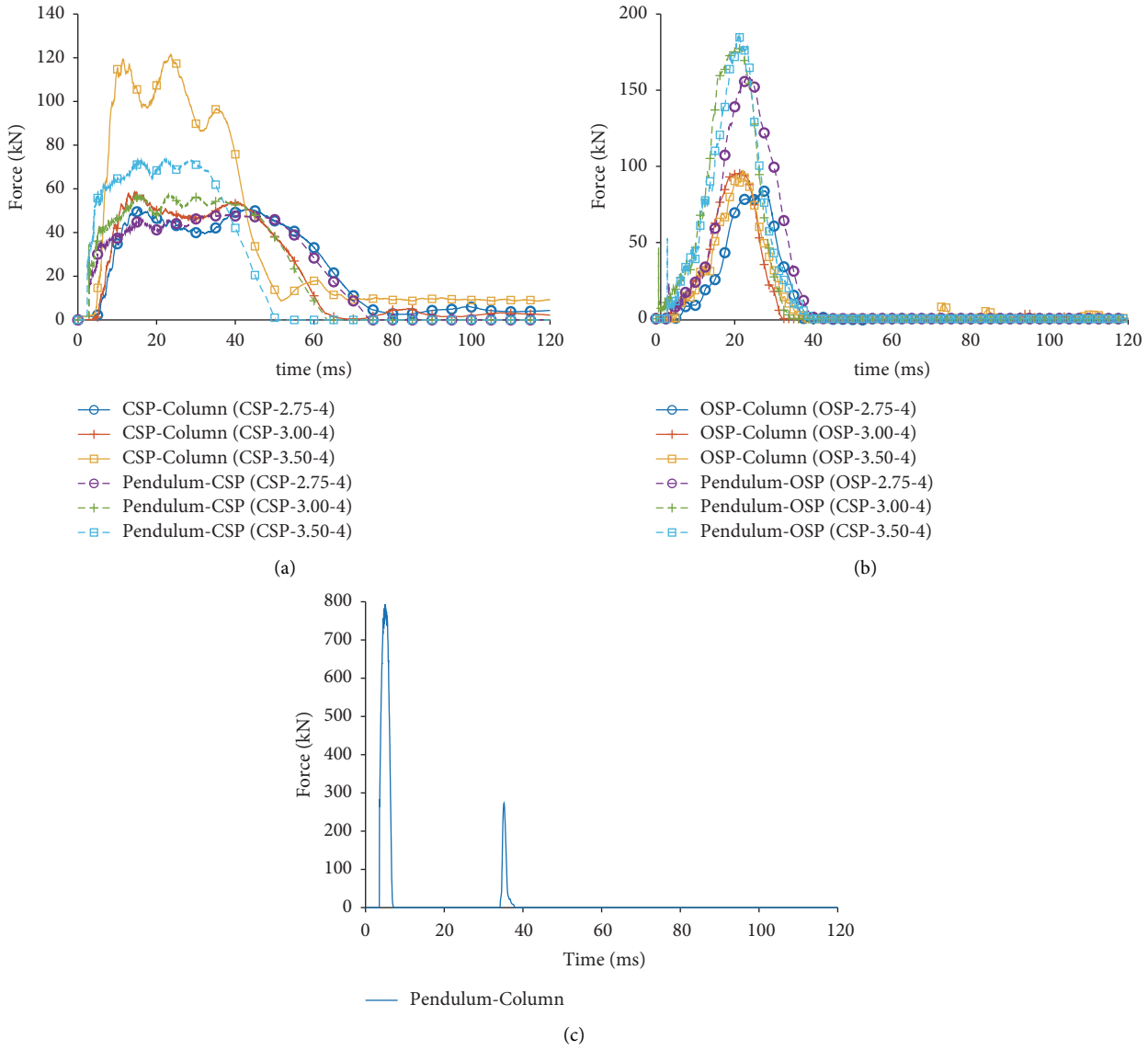

Figure 6: Time history curve of lateral impact force. (a) CSP; (b) OSP; (c) CWACF-12.0-4.

at the top of the column also increases. The smaller the specimen thickness, the smaller the peak value of the lateral displacement at the top of column. When the impact velocity is 2 m/s, the lateral displacement peak value at the top of the column equipped with OSP is smaller than that of the column equipped with CSP. When the impact velocity is 3 and 4 m/s, the lateral displacement peak value of the top of the column equipped with OSP is larger than that of the column equipped with CSP.

3.2. Characteristics of the Lateral Impact Force. Taking the direction that is balanced with the initial impact velocity as the positive direction of the lateral impact force, after numerical simulation, the time history curve of the lateral impact force of each case is obtained. Taking the impact velocity of 4 m/s as an example, the time history curves of the lateral impact force are shown in Figure 6. The peak values of time history curves of the lateral impact force of each case are summarized in Table 3. The results show that the assembly of CSP/OSP can prolong the impact time and reduces the peak value of the lateral impact force. The peak values of the lateral impact force between CSP and pendulum or column are similar, while the force between OSP and pendulum is larger than that of column. The data show that the peak value of lateral impact force of column equipped with OSP is not significantly affected by the change of specimen thickness, but the column equipped with CSP is significantly affected. The smaller the specimen thickness, the smaller the peak value of the lateral impact force of column. When the impact velocity is small, OSP is more effective than CSP in reducing the peak value of the lateral impact force of the column. When the impact velocity is high, CSP can effectively reduce the peak impact force on the column compared to OSP. CSP/OSP specimen can effectively reduce the peak value of lateral impact force of

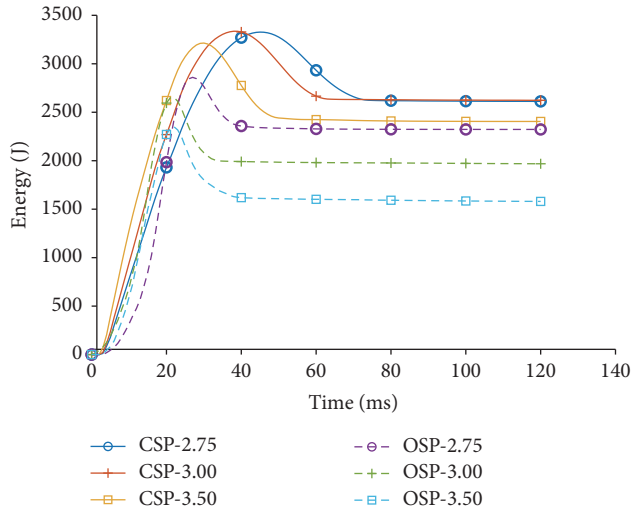

Figure 7: The time history curves of the total energy of CSP/OSP specimen when $V = 4$ m/s.

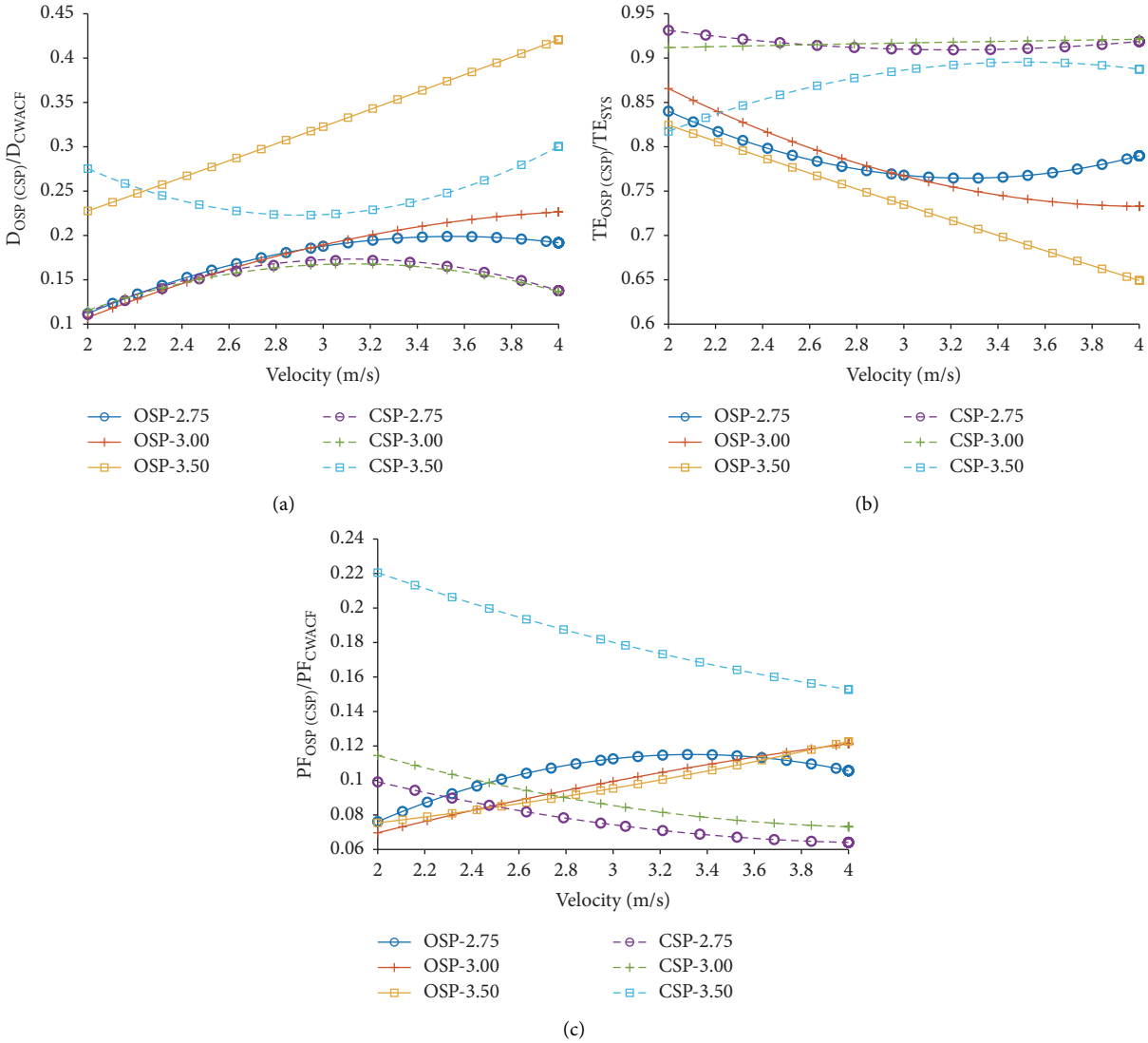

Figure 8: Influence curves of impact velocity. (a) Ratio of lateral displacement peak value at the top of the column. (b) Ratio of total energy peak value of the CSP/OSP specimen. (c) Ratio of lateral impact force peak value.

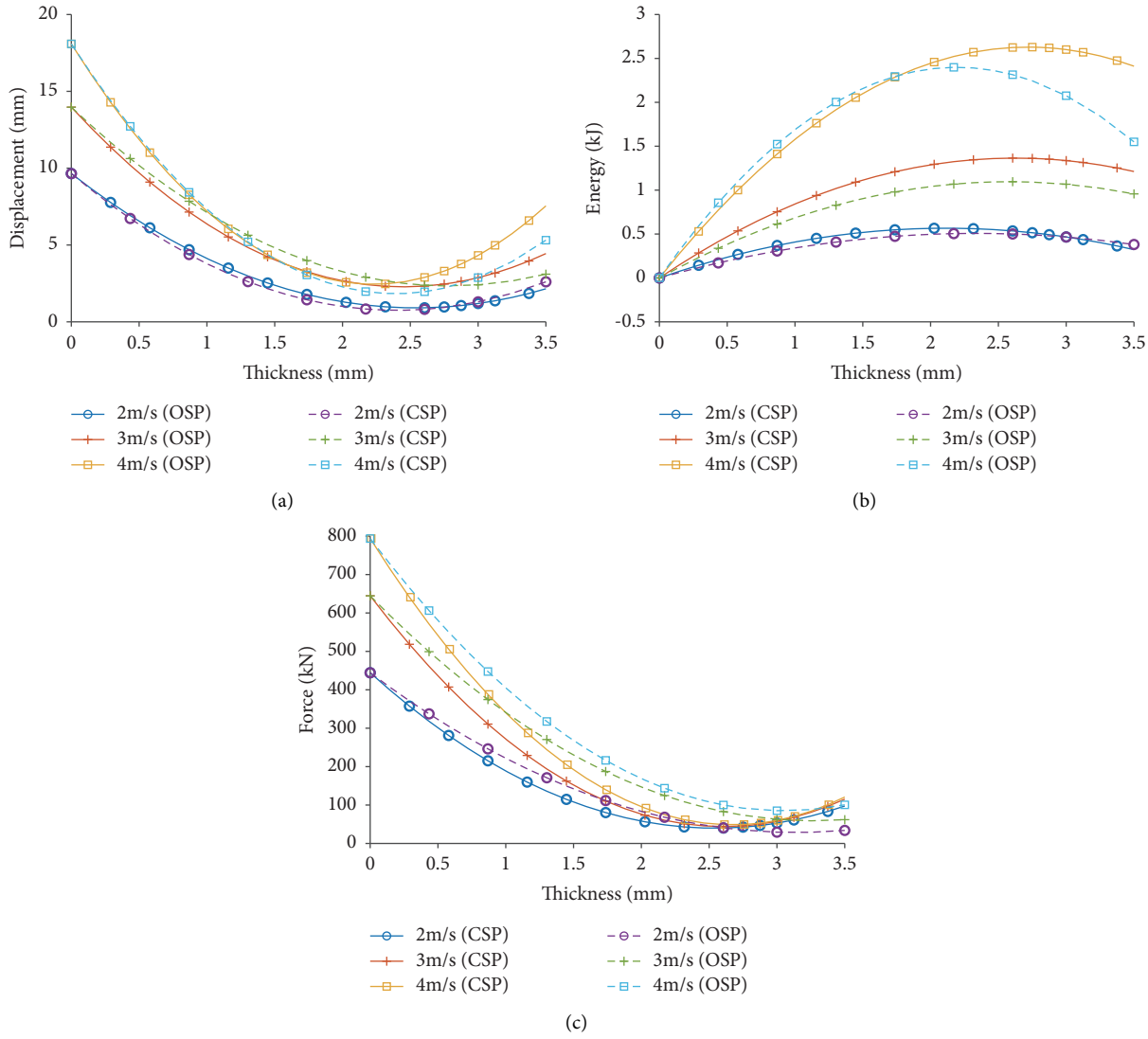

FIGURE 9: Influence curves of specimen thickness. (a) Lateral displacement peak value of the top of the column. (b) Total energy peak value of the CSP/OSP specimen. (c) Lateral impact force peak value.

column. When the specimen thickness is constant, the peak value of the lateral impact force of column increases gradually with the increase of impact velocity.

3.3. The Total Energy of CSP/OSP Specimen. The numerical analysis process follows the law of conservation of energy, and the time history curve of the total energy (kinetic energy + internal energy) of the CSP/OSP specimen is obtained by simulation. Taking the impact velocity of 4 m/s as an example, the time history curves of the total energy of the CSP/OSP specimen are shown in Figure 7. The total energy peak value of CSP/OSP specimen decreases with the increase in the thickness of the specimen and finally it tends to a stable value. The total energy absorbed by CSP specimen is greater than that of OSP specimen. When the impact velocity is 2, 3, and 4 m/s, the total energy of the model system is 908.04, 2043.1, and 3632.16 J, respectively. The results show that the CSP/OSP specimens have obvious energy dissipation effects. With the increase of impact velocity, the total energy absorbed by CSP/OSP also increases, and CSP absorbs more total energy than OSP. Therefore, CSP/OSP specimens have obvious energy dissipation effect, and the of CSP specimen is stronger than the OSP one. The percentage of the total energy peak values of the CSP specimens is greater than that of the OSP specimens.

4. Peak Analysis

To further investigate the anticollision performance of CSP/OSP, the impact velocity, specimen thickness, specimen weight, and specimen frequency effects on each peak values were studied, and the structure and energy dissipation effect of CSP/OSP are evaluated and optimized.

4.1. Impact Velocity. The curves of the ratio of the lateral displacement peak value at the top of the CSP/OSP column ($D_{OSP(CSP)}$) to that of the CWACF column (D_{CWACF}) are shown in Figure 8(a). When the impact velocity is small, the

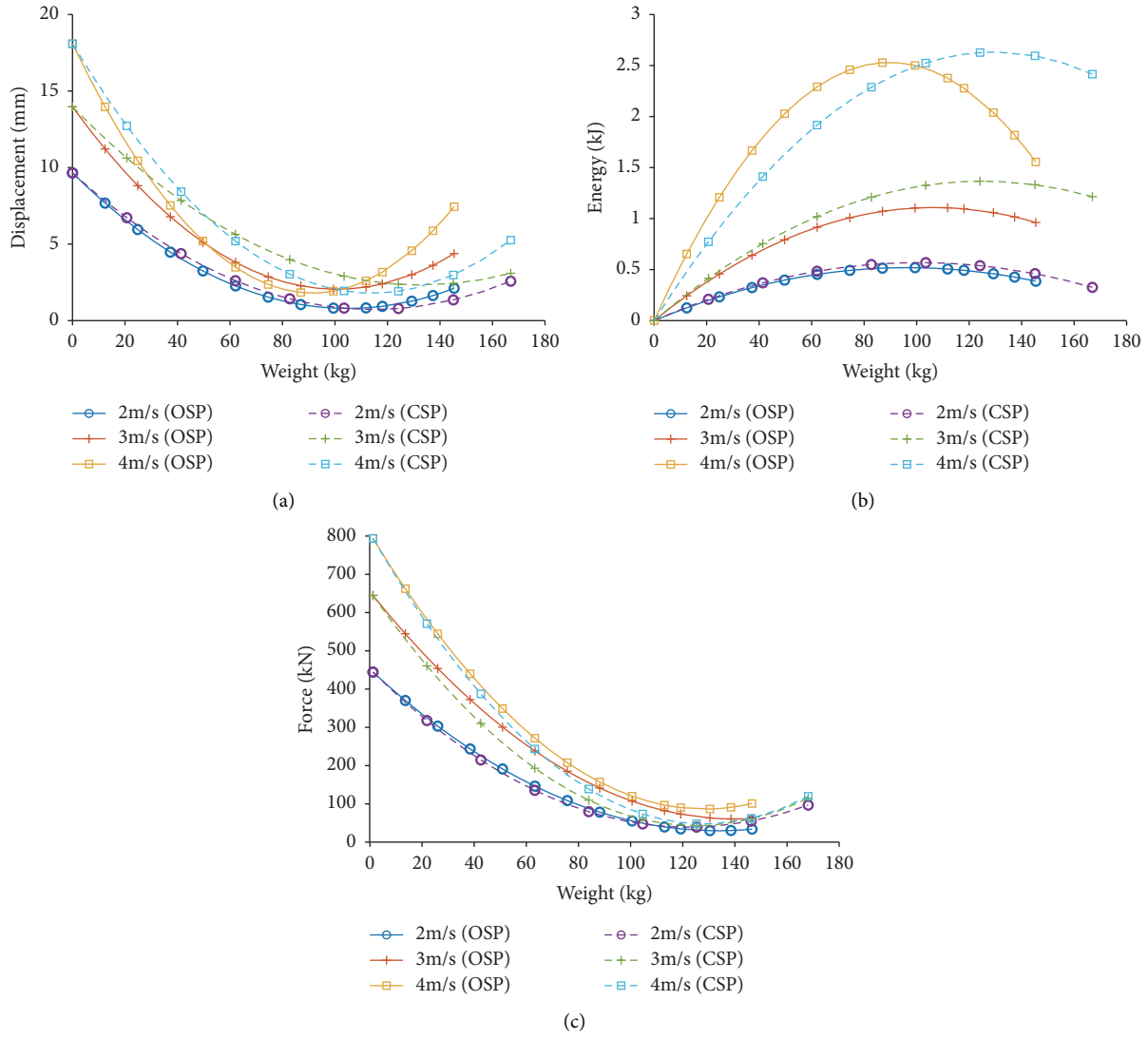

FIGURE 10: Influence curves of specimen weight. (a) Lateral displacement peak value of the top of the column. (b) Total energy peak value of the CSP/OSP specimen. (c) Lateral impact force peak value.

lateral displacement peak value ratio of CSP/OSP is basically close, but that of OSP-3.50 is less than that of CSP-3.50. When the impact velocity is large, the lateral displacement peak value ratio of CSP is small than that of OSP.

The curves of the ratio of the total energy peak value of CSP/OSP specimen ($TE_{OSP(CSP)}$) to that of the model system (TE_{SYS}) are shown in Figure 8(b). The total energy peak value ratios of CSP-2.75 and CSP-3.00 are basically similar, but both are larger than those of CSP-3.50 and OSP. With the increase of impact velocity, the total energy peak value ratio of CSP tends to be stable, while that of OSP gradually decreases. Therefore, CSP/OSP can absorb most of the kinetic energy, and the proportion of CSP absorption is greater than that of OSP.

The curves of the ratio of the lateral impact force peak value of the CSP/OSP column ($PF_{OSP(CSP)}$) to that of the CWACF column (PF_{CWACF}) are shown in Figure 8(c). The lateral impact force peak value ratio of CSP decreased with the increase of impact velocity, but that of the OSP increases with the increase of impact velocity. The ratio of CSP-3.50 is the largest. But when the impact velocity is small, the ratio of CSP is larger than that of OSP. When the impact velocity is large, the ratio of CSP is small than that of OSP.

4.2. Specimen Thickness. The curves of specimen thickness effect on the lateral displacement peak value, the total energy peak value of CSP/OSP specimen, and the lateral impact force peak value are shown in Figures 9(a)–9(c), respectively. The influence curves of specimen thickness are all quadratic curves and have extreme points. With the increase of specimen thickness, the peak values of lateral impact force and lateral displacement first decrease and then increase, while the peak value of total energy first increases and then decreases.

When the impact velocity is 2 m/s, the curve of the lateral displacement peak value of CSP intersects with that of OSP at (0, 9.65), (2.81, 1.00). Within [0, 2.81], the lateral

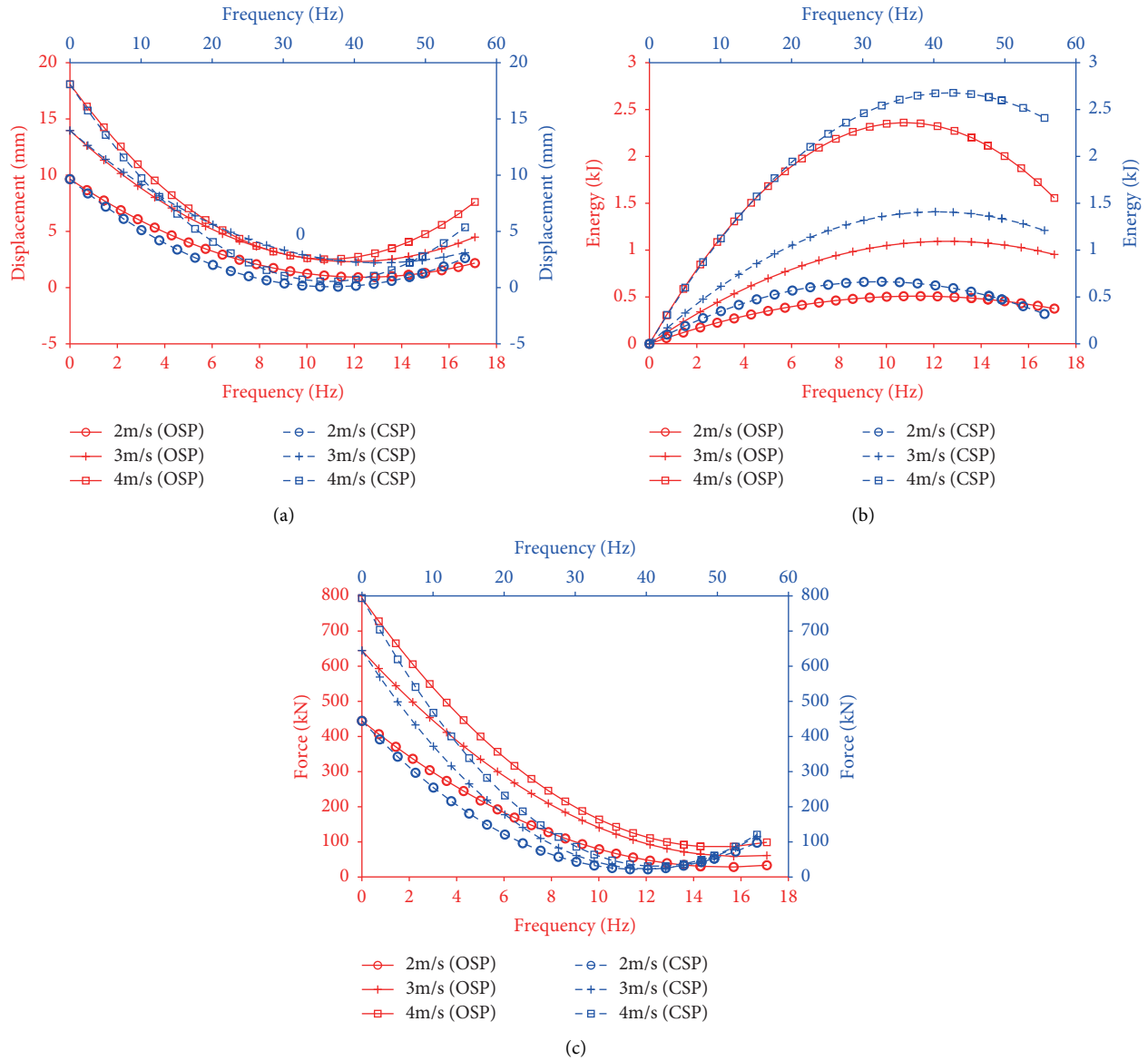

Figure 11: Influence curves of specimen frequency. (a) Lateral displacement peak value of the top of the column. (b) Total energy peak value of the CSP/OSP specimen. (c) Lateral impact force peak value.

displacement peak value of CSP is smaller than that of OSP, but within [2.81, 3.50], the lateral displacement peak value of CSP is larger than that of OSP. The curve of the total energy peak value of CSP specimen intersects with that of OSP at (0, 0), (3.00, 0.466). Within [0.00, 3.00], the total energy peak value of CSP specimen is larger than that of OSP, but, within [3.00, 3.5], the total energy peak value of CSP specimen is smaller than that of OSP. The curve of lateral impact force peak value of CSP intersects with that of OSP at (0,444.39), (2.61, 40.35). Within [0 2.61], the peak value of the lateral impact force of CSP is smaller than that of OSP, but, within [2.61 3.5], the peak value of the lateral impact force of CSP is larger than that of OSP.

When the impact velocity is 3 m/s, the curve of the lateral displacement peak value of CSP intersects with that of OSP at (0, 13.97), (2.66, 2.37). Within [0.00 2.66], the lateral displacement peak value of CSP is larger than that of OSP, but, within [2.66, 3.50], the lateral displacement peak value of CSP is smaller than that of OSP. The curve of the total energy peak value of CSP specimen intersects with that of OSP specimen at (0, 0). Within [0 3.50], the total energy peak value of CSP specimen is larger than that of OSP specimen. The curve of the lateral impact force peak value of CSP intersects with that of OSP at (0,664.63), (3.05, 61.43). Within [0 3.05], the lateral impact force peak value of CSP is smaller than that of OSP, but, within [3.05 3.5], the lateral impact force peak value of CSP is larger than that of OSP.

When the impact velocity is 4 m/s, the curve of the lateral displacement peak value of CSP intersects with that of OSP at (0, 18.08), (1.46, 4.28). Within [0.1.46], the lateral displacement peak value of CSP is slightly larger than that of OSP, but, within [1.46, 3.5], the lateral displacement peak

value of CSP is smaller than that of OSP. The curve of total energy peak value of CSP specimen intersects with that of OSP at (0,0), (1.76, 2.31). Within [0, 1.76], the total energy peak value of CSP specimen is smaller than that of OSP, but, within [1.76, 3.50], the total energy peak value of CSP specimen is larger than that of OSP. The curve of the lateral impact force peak value of CSP intersects with that of OSP at (0,793.69), (3.31, 90.25). Within [0 3.31], the lateral impact force peak value of CSP is larger than that of OSP, but, within [3.31 3.5], the lateral impact force peak value of CSP is smaller than that of OSP.

4.3. Specimen Weight. The influence curves of specimen weight effect on the lateral displacement peak value at the top of the column, the total energy peak vale of CSP/OSP specimen, and the lateral impact force peak value are shown in Figures 10(a)–10(c), respectively. The influence curves of specimen weight are all quadratic curves and have extreme points. With the increase of the specimen weight, the lateral displacement peak value at the top of the column and the lateral impact force first decreased and then increased, while the total energy peak value of CSP/OSP specimen first increased and then decreased.

When the impact velocity is 2 m/s, the curves of column lateral displacements of CSP and OSP intersect at (0, 9.64), (105.88, 0.78). Within [0.00, 105.88], the lateral displacement peak value of CSP is larger than that of OSP, but, within [105.88, 166.96], the lateral displacement peak value of CSP is smaller than that of OSP. The total energy peak value of CSP specimen intersects with that of OSP at (0, 0). Within [0.00 166.957], the total energy peak of CSP specimen is larger than that of OSP. The lateral impact force peak value of CSP intersects with that of OSP at (0, 444.46), (108.11, 43.58). Within [0.00, 108.11], the lateral impact force peak value of CSP is smaller than that of OSP. Within [108.11, 166.96], the lateral impact force peak value of CSP is larger than that of OSP.

When the impact velocity is 3 m/s, the lateral displacement peak value of CSP intersects with that of OSP at (0, 13.97), (119.19, 2.45). Within [0, 119.19], the lateral displacement peak value of CSP is larger than that of OSP, but, within [119.19, 166.96], the lateral displacement peak value of CSP is smaller than that of OSP. The total energy peak value of the CSP specimen intersects with that of OSP specimen at (0, 0). Within [0, 166.81], the total energy peak value of CSP specimen is larger than that of OSP specimen. The lateral impact force peak value of CSP intersects with that of OSP at (0, 664.71), (145.39, 60.44). Within [0 145.39], the lateral impact force peak value of CSP is smaller than that of OSP, but, within [145.39, 166.96], the lateral impact force peak value of CSP is larger than that of OSP.

When the impact velocity is 4 m/s, the lateral displacement peak value of CSP intersects with that of OSP at (0, 18.09), (100.71, 2.03). Within [0, 100.71], the lateral displacement peak value of CSP is larger than that of OSP, but, within [100.71, 166.96], the lateral displacement peak value of CSP is smaller than that of OSP. The curve of total energy peak value of the CSP specimen intersects with that of OSP specimen at (0, 0), (99.98, 2.49). Within [0 99.98], the total energy peak value of CSP specimen is smaller than that of OSP specimen, but, within [99.98, 166.96], the total energy peak value of CSP specimen is smaller than that of OSP specimen. The curve of lateral impact force peak value of CSP intersects with that of OSP at (0, 793.69). Within [0 166.96], the lateral impact force peak value of CSP is smaller than that of OSP.

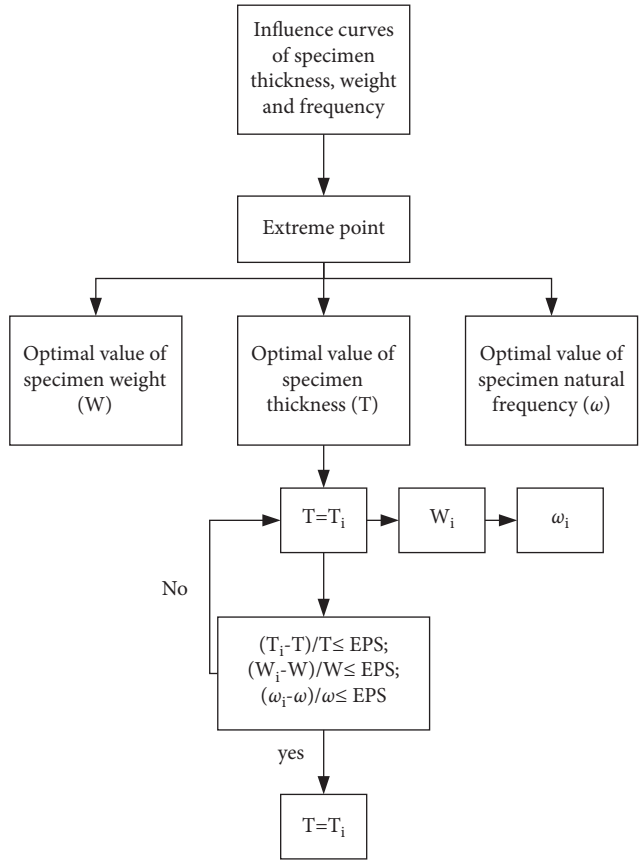

Figure 12: Technical route of structural optimization.

4.4. Specimen Frequency. The influence curves of CSP/OSP specimen frequency [40] effect on the lateral displacement peak value at the top of the column, the total energy peak value of CSP/OSP specimen, and the lateral impact force peak value off the column are shown in Figures 11(a)–11(c), respectively. The influence curves of specimen frequency are all quadratic curves and have extreme points. With the increase of specimen frequency, the lateral displacement peak value at the top of the column and the lateral impact force peak value of the column decrease first and then increase. The total energy peak values of CSP and OSP specimens first increase and then decrease. The curves change rate of OSP is greater than that of CSP.

4.5. Structural Optimization. The influence curves of CSP/OSP specimens thickness, weight, and frequency are analysed in Sections 4.2–4.4. However, each curve presents a quadratic curve with extreme points. Therefore, the technical

Table 4: Optimization results.

Type	Category	Parameter		Ratio	Impact velocity (m/s)	Lateral displacement peak value		Lateral impact force peak value		Total energy peak value of CSP/OSP specimen		Total energy peak value of the column	
		Optimal value	Calculated value			Simulation (mm)	Percentage (%)	Simulation (kN)	Percentage (%)	Simulation (J)	Percentage (%)	Simulation (J)	Percentage (%)
CSP	Thickness (mm)	2.71	2.5	0.92	2	1.87	19.38	31.80	7.16	820.00	90.30	22.60	2.49
	Weight (kg)	134.89	119.41	0.89	3	2.10	15.03	36.80	5.71	1870.00	91.53	29.00	1.42
	Frequency (Hz)	42.55	40.60	0.95	4	2.18	12.06	39.40	4.96	3350.00	92.23	31.70	0.87
OSP	Thickness (mm)	2.83	2.5	0.88	2	1.12	11.61	37.00	8.33	768.00	84.58	17.70	1.95
	Weight (kg)	122.09	107.58	0.88	3	2.82	20.19	65.20	10.11	1600.00	78.31	92.70	4.54
	Frequency (Hz)	13.85	12.20	0.88	4	3.38	18.69	91.90	11.58	2960.00	81.49	122.00	3.36

route of CSP/OSP structure optimization is shown in Figure 12, and the optimization results are summarized in Table 4.

The results show that when the impact energy is low, the lateral displacement peak value of the top of the column, the lateral impact force peak value of the column, and the total energy peak value of the column equipped with OSP are smaller than those of the column equipped with CSP. When the impact energy is high, the lateral displacement peak value of the top of the column equipped with OSP, the lateral impact force peak value of the column equipped with OSP, and the total energy peak value of the column equipped with OSP are all larger than those of the column equipped with CSP. However, under the same impact energy, the total energy peak value of the CSP specimen is larger than that of the OSP specimen. The total energy peak value of the CSP specimen accounts for more than 90.30% of the total energy of the model system, whereas the total energy peak value of the OSP specimen accounts for more than 78.31% of the total energy of the model system. Therefore, using CSP is recommended.

5. Conclusion

The numerical model verified by the pendulum impact test is used to simulate the whole process of the impact test, and the time history curve and its peak value of the simulation results are obtained. Then, the influence curves of the impact velocity, specimen thickness, weight, and frequency are analysed, and the following conclusions are obtained:

(1) According to the pendulum impact test, the corresponding simplified establishment method of numerical model is proposed, and the simulation results are basically consistent with the test results.

(2) The anticollision performance of CSP/OSP specimens is compared and analysed. Under the same impact energy, the energy absorbed by the CSP specimen is greater than that of the OSP specimen. Therefore, using CSP is recommended.

(3) The method of establishing the numerical model has been verified by the impact test. In the next step, the numerical simulation on the anticollision performance of the overall structure of the new corrugated steel protection system can be carried out.

Data Availability

The data used to support the findings of this study are included within the article.

Disclosure

The opinions, findings, and conclusions do not reflect the opinions of the funding agencies or other individuals.

Conflicts of Interest

There are no conflicts of interest regarding the publication of this paper.

Acknowledgments

The authors are grateful for the support from the School of Civil Engineering, Chongqing Jiaotong University, State Key Laboratory of Mountain Bridge and Tunnel Engineering, and State Key Laboratory of Mountain Bridge and Tunnel Engineering Co-built by Provincial Government and the Ministry of Transport. The first author acknowledges the Research Project of the Ministry of Transport of the People's Republic of China (no. 2011318223190) for funding the research of this article. Special thanks are due to Dr. Haiyang Yi for his assistance in the writing and translation of the paper and to Nanjing PMLAB∗ Sensor Tech. Co., Ltd. for the assistance during the test data collection.

References

[1] M. A. Knott, "Vessel Collision Design Codes and Experience in the United States [J]," *Ship Collision Analysis*, Routledge, England, UK, 1998.

[2] E. V. Manen and A. G. Frandsen, "Ship Collision with Bridges, Review of Accidents [J]," *Ship Collision Analysis*, Routledge, England, UK, 1998.

[3] A. Lrfd, *Bridge Design Specifications*, American Association of State Highway and Transportation Officials, Washington, DC, USA, 8th edition, 2017.

[4] G. Chen, "Summarize of the research and design on anti-collision ship with bridge for 30 years in China," shanghai association of old scientific and technical workers," in *Proceedings of the 9th Annual Conference of Shanghai Association of Old Science and Technology Workers Shanghai Ocean Steel Structure Research Institute*, pp. 253–259, Shanghai, China, February 2011.

[5] C. E. N. G. Peng, "Protection of bridge piers against ship collision [J]," *Steel Construction*, vol. 2, no. 1, pp. 21–32, 2010.

[6] G. Chen, "New equipment of ship collision with the pier and its mechanism research," *Ship Engineering*, vol. 29, no. 4, pp. 40–43, 2007.

[7] H. Jiang, Bo Geng, and X. X. Zhang, "A new fender system for bridge pier protection against vessel collision," *Journal of Vibration and Shock*, vol. 33, no. 17, pp. 154–160, 2014.

[8] X. Zhou, Z. Hu, and Yu Zhao, "Research on anti-collision performance of combined anti-collision box," *Journal of Wuhan University of Technology*, vol. 41, no. 2, pp. 662–667, 2017.

[9] C. Shan and Z. Huang, "Collision performance analysis of curved-shaped anti-collision floating box of bridge pier with sandwich structure," *Journal of South China University of Technology*, vol. 47, no. 2, pp. 662–667, 2019.

[10] Y. Y. Chen, T. T. Li, Z. Jia, F. Scarpa, C. W. Yao, and L. Wang, "3D printed hierarchical honeycombs with shape integrity under large compressive deformations," *Materials & Design*, vol. 137, pp. 226–234, 2018.

[11] M. Stanczak, T. Fras, L. Blanc, P. Pawlowski, and A. Rusinek, "Blast-induced compression of a thin-walled aluminum honeycomb structure-experiment and modeling," *Metals*, vol. 9, no. 12, p. 1350, 2019.

[12] T. Wang, Z. Li, and L. M. Wang, "Dynamic crushing analysis of a three-dimensional Re-entrant auxetic cellular," *Structure [J]. Materials*, vol. 12, no. 3, p. 15, 2019.

[13] Y. Fang, C. Liu, H. Yang, and L Yang, "Axial behaviour of concrete-filled corrugated steel tubular column embedded

with structural steel," *Journal of Constructional Steel Research*, vol. 170, p. 106064, 2020.

[14] M. Nassirnia, A. Heidarpour, X. L. Zhao, and J Minkkinen, "Innovative hollow columns comprising corrugated plates and ultra high-strength steel tubes," *Thin-Walled Structures*, vol. 101, pp. 14–25, 2015.

[15] M. Wojcik, M. Sondej, K. Rejowski, and J Tejchman, "Full-scale experiments on wheat flow in steel silo composed of corrugated walls and columns," *Powder Technology*, vol. 311, pp. 537–555, 2017.

[16] O. Kearns, I. D. Moore, and N. A. Hoult, "Measured responses of a corrugated steel ellipse culvert at different cover depths," *Journal of Bridge Engineering*, vol. 25, no. 11, p. 11, 2020.

[17] D. B. Garcia and I. D. Moore, "Behavior of coupling band joints in buried corrugated steel pipelines," *Journal of Geotechnical and Geoenvironmental Engineering*, vol. 140, no. 2, p. 9, 2014.

[18] D. Beben, "The role of backfill quality on corrugated steel plate culvert behaviour [J]," *The Baltic Journal of Road and Bridge Engineering*, vol. 12, no. 1, pp. 1–11, 2017.

[19] B. J. Li, L. S. Zhu, Y. Li, and X. S. Fu, "Experimental investigation of an existing RCP rehabilitated with a grouted corrugated steel pipe," *Mathematical Problems in Engineering*, vol. 2019, Article ID 7676359, 13 pages, 2019.

[20] C. Regier, I. D. Moore, and N. A. Hoult, "Remaining strength of deteriorated corrugated steel culverts," *Journal of Pipeline Systems Engineering and Practice*, vol. 9, no. 2, p. 15, 2018.

[21] Z. X. Yang, J. Yan, J. L. Chen, Q. Lu, and Q. Yue, "Multi-objective shape optimization design for liquefied natural gas cryogenic helical corrugated steel pipe," *Journal of Offshore Mechanics and Arctic Engineering*, vol. 139, no. 5, p. 11, 2017.

[22] Y. L. Guo, J. S. Zhu, M. Z. Wang, X. Yang, and P. Zhou, "Overall instability performance of concrete-infilled double steel corrugated-plate wall," *Thin-Walled Structures*, vol. 130, pp. 372–394, 2018.

[23] Y. H. Wang, Z. Y. Gao, Q. Han, L. Feng, H. Su, and N. Zhao, "Experimental study on the seismic behavior of a shear wall with concrete-filled steel tubular frames and a corrugated steel plate," *The Structural Design of Tall and Special Buildings*, vol. 27, no. 15, Article ID e1509, 2018.

[24] J. S. Zhu, Y. L. Guo, M. Z. Wang, X. Yang, and Y. L. Pi, "Seismic performance of concrete-infilled double steel corrugated-plate walls: experimental research," *Engineering Structures*, vol. 215, no. 18, Article ID 110601, 2020.

[25] J. S. Zhu, Y. L. Guo, M. Z. Wang, X. Yang, and B. L. Zhu, "Strength design of concrete-infilled double steel corrugated-plate walls under uniform compressions," *Thin-Walled Structures*, vol. 141, pp. 153–174, 2019.

[26] M.-Z. Wang, Y.-L. Guo, J.-S. Zhu, and X. Yang, "Flexural buckling of axially loaded concrete-infilled double steel corrugated-plate walls with T-section," *Journal of Constructional Steel Research*, vol. 166, Article ID 105940, 2020.

[27] M.-Z. Wang, Y.-L. Guo, J.-S. Zhu, and Y. Xiao, "Flexural-torsional buckling and design recommendations of axially loaded concrete-infilled double steel corrugated-plate walls with T-section [J]," *Engineering Structures*, vol. 208, 2020.

[28] M. Leblouba, S. W. Tabsh, and S. Barakat, "Reliability-based design of corrugated web steel girders in shear as per AASHTO LRFD," *Journal of Constructional Steel Research*, vol. 169, Article ID 106013, 2020.

[29] M. Leblouba and S. W. Tabsh, "Reliability-based shear design of corrugated web steel beams for AISC 360 specification and CSA-S16 standard [J]," *Engineering Structures*, vol. 215, 2020.

[30] C. Zhou, L. F. Li, and L. H. Wang, "Improved softened membrane model for prestressed composite box girders with corrugated steel webs under pure torsion," *Journal of Constructional Steel Research*, vol. 153, pp. 372–384, 2019.

[31] M. Zhou and L. An, "Full-range shear behavior of a non-prismatic beam with steel trapezoidal corrugated webs: experimental tests and FE modeling," *Journal of Structural Engineering*, vol. 146, no. 8, p. 14, 2020.

[32] J. He, Y. Q. Liu, X. Q. Xu, and L Li, "Loading capacity evaluation of composite box girder with corrugated webs and steel tube slab," *Structural Engineering & Mechanics*, vol. 50, no. 4, pp. 501–524, 2014.

[33] J. He, S. H. Wang, Y. Q. Liu, Z. Lyu, and C. Li, "Mechanical behavior of a partially encased composite girder with corrugated steel web: interaction of shear and bending," *Engineering*, vol. 3, no. 6, pp. 806–816, 2017.

[34] C. D. Si, X. Su, and E. L. Chen, "Comparative study on dynamic response of deck pavement of two kinds of box girder bridges under moving loads [J]," *Shock and Vibration*, vol. 2019, no. 13, 2019.

[35] M. Maslak, M. Pazdanowski, and M. Suchodola, "Influence of geometrical imperfection on critical temperature evaluation for steel corrugated arch sheets exposed to fire [M]," in *Proceedings of the 64 Scientific Conference of the Committee for Civil Engineering of the Polish Academy of Sciences and the Science Committee of the Polish Association of Civil Engineers (PZITB) (KRYNICA 2018)*, Krynica, Poland, June 2019.

[36] L. L. Wu, L. P. An, and Y. Bai, "In-plane stability of steel circular closed supports with I-section of sinusoidal corrugated webs: experimental and numerical study [J]," *Tunnelling and Underground Space Technology*, vol. 160, no. 14, 2020.

[37] W. Fan, D. J. Shen, Z. Y. Zhang, X. Huang, and X. Shao, "A novel UHPFRC-based protective structure for bridge columns against vehicle collisions: experiment, simulation, and optimization," *Engineering Structures*, vol. 207, no. 21, Article ID 110247, 2020.

[38] Q. H. Zhao, Y. K. Li, Y. Tian, and Z Li, "Cyclic behavior of corrugated double-skin composite walls with different aspect ratios," *Journal of Structural Engineering*, vol. 146, no. 10, p. 18, 2020.

[39] A. Niknejad, Y. Abdolzadeh, J. Rouzegar, and M Abbasi, "Experimental study on the energy absorption capability of circular corrugated tubes under lateral loading and axial loading," *Proceedings of the Institution of Mechanical Engineers - Part D: Journal of Automobile Engineering*, vol. 229, no. 13, pp. 1739–1761, 2015.

[40] G. Chen, H. Huang, and Z. Xiang, "Experimental investigation on the anticollision performance of corrugated steel-reinforced composites for bridge piers," *Shock and Vibration*, vol. 2021, pp. 1–17, 2021.

[41] De-jin Huang, Li-li Wang, and Ni Bu-you, "The numerical analysis and experiment of synchronism on multi-anti-collision ring within the anti-collision device with outer steel gate," in *Proceedings of the International Symposium on Ship-Bridge Collision and its Protection*, pp. 146–153, 2014.

[42] X. Zhang, H. Hao, and C. Li, "Experimental investigation of the response of precast segmental columns subjected to impact loading," *International Journal of Impact Engineering*, vol. 95, pp. 105–124, 2016.

[43] T. V. Do, T. M. Pham, and H. Hao, "Dynamic responses and failure modes of bridge columns under vehicle collision," *Engineering Structures*, vol. 156, pp. 243–259, 2018.

[44] W. Zhang and Y. Hu, "Numerical simulation method for high-strength bolt connections in steel structures," *Journal of Harbin Institute of Technology*, vol. 46, pp. 8–14, 2014.
[45] B. Wen, *Mechanical Design Handbook [M]*, Machinery Industry Press, South Norwalk, Connecticut, 6th edition, 2020.
[46] X. Zhi, R. Zhang, Li Lin, and F. Fan, "Dynamic constitutive model of Q235 steel and its application in LS-DYNA," *Explosion and Shock Waves*, vol. 38, no. 3, pp. 596–602, 2018.
[47] D. K. Kim, W. C. K. Ng, and O. Hwang, "An empirical formulation to predict maximum deformation of blast wall under explosion [J]," *Structural Engineering & Mechanics*, vol. 68, no. 2, pp. 237–245, 2018.
[48] J. K. Paik, B. J. Kim, and S. K. Park, "On the crashworthiness of steel-plated structures in an arctic environment: an experimental and numerical study," in *Proceedings of the ASME 2010 29th International Conference on Ocean, Offshore and Arctic Engineering*, American Society of Mechanical Engineers (ASME), Shanghai, China, June 2010.
[49] D. K. Park, D. K. Kim, and C.-H. Park, "On the crashworthiness of steel-plated structures in an arctic environment: an experimental and numerical study [J]," *Journal of Offshore Mechanics and Arctic Engineering*, vol. 137, no. 5, 2015.
[50] A. Rokaya and J. Kim, "An accurate analysis for sandwich steel beams with graded corrugated core under dynamic impulse," *Int J Steel Struct*, vol. 18, no. 5, pp. 1541–1559, 2018.